Nano Res. 2012, 5(9): 605–617
DOI 10.1007/s12274-012-0246-X
Research Article

ISSN 1998-0124
CN 11-5974/O4

Graphene–Nickel Cobaltite Nanocomposite Asymmetrical Supercapacitor with Commercial Level Mass Loading

Huanlei Wang[1,2], Chris M. B. Holt[1,2], Zhi Li[1,2] (✉), Xuehai Tan[1,2], Babak Shalchi Amirkhiz[1,2], Zhanwei Xu[1,2], Brian C. Olsen[1,2], Tyler Stephenson[1,2], and David Mitlin[1,2] (✉)

[1] Chemical and Materials Engineering, University of Alberta, Edmonton, Alberta T6G 2V4, Canada
[2] National Institute for Nanotechnology (NINT), National Research Council of Canada, Edmonton, Alberta T6G 2M9, Canada

Received: 23 June 2012 / Accepted: 15 July 2012

ABSTRACT

A high performance asymmetric electrochemical supercapacitor with a mass loading of 10 mg·cm^{-2} on each planar electrode has been fabricated by using a graphene–nickel cobaltite nanocomposite (GNCC) as a positive electrode and commercial activated carbon (AC) as a negative electrode. Due to the rich number of faradaic reactions on the nickel cobaltite, the GNCC positive electrode shows significantly higher capacitance (618 F·g^{-1}) than graphene–Co_3O_4 (340 F·g^{-1}) and graphene–NiO (375 F·g^{-1}) nanocomposites synthesized under identical conditions. More importantly, graphene greatly enhances the conductivity of nickel cobaltite and allows the positive electrode to charge/discharge at scan rates similar to commercial AC negative electrodes. This improves both the energy density and power density of the asymmetric cell. The asymmetric cell composed of 10 mg GNCC and 30 mg AC displayed an energy density in the range of 19.5 Wh·kg^{-1} with an operational voltage of 1.4 V. At high sweep rate, the system is capable of delivering an energy density of 7.6 Wh·kg^{-1} at a power density of about 5600 W·kg^{-1}. Cycling results demonstrate that the capacitance of the cell increases to 116% of the original value after the first 1600 cycles due to a progressive activation of the electrode, and maintains 102% of the initial value after 10000 cycles.

KEYWORDS

Graphene, nickel cobaltite ($NiCo_2O_4$), supercapacitor, energy density, power density

1. Introduction

An electrochemical capacitor, also known as a supercapacitor or an ultracapacitor, stores energy via near-surface ion adsorption, with an additional possible contribution from fast reversible Faradic reactions [1–4]. Such devices can fill the gap between batteries and conventional solid state and electrolytic capacitors, providing a much higher power density and longer cycle life than the former, and a much higher energy density than the latter. High performance electrochemical capacitors are very important for electric vehicles and hybrid electric vehicles. Although high power uptake (~10 to 10^4 W·kg^{-1}) can be achieved for electrochemical capacitors, their energy density (~0.2 to 10 Wh·kg^{-1}) is significantly lower than those of batteries (~10 to 200 Wh·kg^{-1}) [5]. Therefore, a key goal for the development of electrochemical capacitors is to improve their energy density while maintaining high power density and long cycle life. According to

Address correspondence to David Mitlin, dmitlin@ualberta.ca; Zhi Li, lizhicn@gmail.com

the following equation $E = 0.5 \cdot C \cdot V^2$, where E is the energy density, C is the capacitance of electrochemical capacitor, and V is the cell voltage, the energy density of an electrochemical capacitor can be enhanced by either maximizing the specific capacitance or increasing the cell voltage [6]. A promising way to improve the cell voltage in aqueous-based electrochemical capacitors is to use asymmetric electrodes, where the oxygen evolution reaction on the oxide-based positive electrode is suppressed [7, 8].

Recently, considerable research efforts have been devoted to various asymmetric electrochemical capacitor systems [9–12]. Carbon materials are widely utilized for negative electrodes in asymmetric electrochemical capacitors due to their high surface area, high conductivity and stable physical and chemical properties. Porous carbons with high surface area and interconnected pore structure can be beneficial for charge accumulation and ion transportation, resulting in enhanced energy density and excellent rate capability [13–16]. Metal oxide materials are suitable for pseudocapacitive electrodes in asymmetric systems. Among them, RuO_2 is the most prominent material due to its high electrical conductivity and high specific capacitance [17], however, the high cost of Ru is a limitation for practical application. Less expensive oxides and nitrides have been extensively utilized for capacitors [18–22]. The charge storage mechanism of these metal oxides is based on fast redox reactions occurring on the electrode/electrolyte surface. Since the electrical conductivity of most metal oxides is poor, using carbon–metal oxide composites is a common and promising way to increase the conductivity and further improve the power density [23–25].

Graphene is considered an attractive electrode material due to its superior electrical conductivity, high theoretical surface area, and good electrochemical stability [26–28]. Graphene-based composites with metal oxides or conducting polymer have been successfully synthesized for supercapacitors [29–31]. These and similar studies demonstrated that graphene possesses a dual role, to disperse metal oxide or polymer at the nanoscale and to act as a highly conductive matrix for enhancing the electrical conductivity of the electrode. Recently there have been some promising studies on the graphene–NiO, and graphene–Co_3O_4 systems [32–34]. In binary nickel cobaltite ($NiCo_2O_4$), the co-existence of nickel and cobalt ions can offer a richer variety of redox reactions, resulting in enhanced electrochemical performance relative to NiO or Co_3O_4 [35, 36]. Despite the promise for excellent electrochemical performance, to date little work has been done in combining $NiCo_2O_4$ with graphene at the nanoscale. In the only previous study [37] the authors exfoliated layered double hydroxides and graphene oxide resulting in a heteroassembly of oppositely charged nanosheets, followed by co-reduction. However, this process is complicated. The approach utilized in our study is a facile hydrothermal process consisting of 100 ˚C solution treatment of precursors and commercial graphene nanoplatelets followed by low temperature calcination in air. The obtained graphene–nickel cobaltite composite can be charged/discharged at high scan rates with high reversibility. There are only a limited number of studies that have treated graphene-based asymmetric capacitors. Hybrid graphene–MnO_2 nanowire composite//graphene, graphene–RuO_2//graphene–polyaniline, graphene–$Ni(OH)_2$//graphene–RuO_2, and graphene–MnO_2// activated carbon asymmetric capacitors have been developed. Although high energy density is achieved in these studies, the cyclability could be further improved [9, 30, 38, 39].

Herein we fabricate a novel asymmetric capacitor based on a graphene–nickel cobaltite nanocomposite positive electrode, and a commercial activated carbon negative electrode. There are several unique aspects in this work: first, despite its significant promise compared with the extensively studied graphene–metal oxide combinations, the graphene–nickel cobaltite ($NiCo_2O_4$) nanocomposite remains poorly explored. Second, we demonstrate a uniquely favorable electrical conductivity and cycling lifetime that is accomplished by combining the nickel cobaltite with graphene at the nanoscale. While a high energy density is achievable in an unsupported oxide, it is almost always at the expense of the device power density due to the high equivalent series resistance of the electrode. To paraphrase Conway et al., by introducing a "high-capacity" oxide-based electrode, researchers inevitably transform good supercapacitors

into mediocre batteries [1]. We show that by incorporating a nanodispersed skeleton of graphene into the oxide, a high electrical conductivity is maintained even for very thick electrodes. This allows for power density–energy density combinations that are among the best reported for an aqueous electrolyte-based device (5600 $W \cdot kg^{-1}$ at 7.6 $Wh \cdot kg^{-1}$). Furthermore the graphene skeleton completely prevents cycling-induced degradation: after 10000 cycles the capacitance of the cell is actually 102% of the initial value. Such stability is quite rare in any oxide-based system.

Due to the poor electrical conductivity of metal oxides, their specific capacitances are very sensitive to the mass of active material and thickness of the electrode. Exaggerated specific capacitances can be obtained when using extremely thin or low mass loadings and these decrease quickly with electrode thickness [40]. To increase the *geometric surface area* mass loadings, researchers have typically coated a thin layer of electroactive materials onto highly porous three-dimensional (3-D) substrates, such as Ni foams or carbon cloths that are millimeters in thickness [20, 41, 42]. This technique works well for applications where the geometric surface area of an electrode is the main consideration rather than the mass. However, this approach is not the best choice to make real supercapacitors since those substrates significantly increase the dead mass of an electrode. It has been recently demonstrated that to obtain realistic capacitance values electrode materials should be tested in a similar manner to a commercial electrode, with a mass loading on the order of 10 $mg \cdot cm^{-2}$ [43, 44]. To meet this key requirement we fabricated an asymmetric cell employing an active material mass loading *per real surface area* of 10 $mg \cdot cm^{-2}$. This is the third unique aspect of this study, and is attributable to the role of the graphene network in maintaining high electrical conductivity even at commercial-level electrode mass loadings.

2. Experimental

2.1 Preparation of graphene–nickel cobaltite composite

Graphene nanoplatelets were purchased from Cheap Tubes Inc. They were designated "Grade 3", having an average thickness of less than 8 nm and a surface area of 670 $m^2 \cdot g^{-1}$. The platelets were treated with concentrated HNO_3 for 20 h. The acid-treated graphene material (0.1 g) was dispersed in 100 mL of deionized water, followed by the addition of hexadecyltrimethylammonium bromide (CTAB, 1 g), urea, nickel nitrate hexahydrate, and cobalt chloride hexahydrate. The molar ratio of Ni^{2+}:Co^{2+}:urea was 1:2:45. The mixture was transferred into a sealed container and treated under sonication for 1 h. After sonication, the solution was heated to 100 ℃ under stirring for 6 h. The resulting precursor was collected and washed with deionized water, and dried at 100 ℃ in an oven. Afterward, the dried sample was calcined at 250 ℃ or 350 ℃ for 3 h in air.

2.2 Characterization techniques

X-ray diffraction (XRD) analysis was performed using a Bruker AXS D8 Discover diffractometer with Cu Kα radiation. Transmission electron microscopy (TEM) analysis was performed using a JEOL JEM-2010 transmission electron microscope with an accelerating voltage of 200 kV. Scanning electron microscopy (SEM) analysis was conducted using a Hitachi S-4800 field emission scanning microscope. X-ray photoelectron spectroscopy (XPS) analysis was performed using an Axis Ultra spectrometer with a base pressure of 5×10^{-10} Torr. The specific surface area and pore structure were investigated using a Quantachrome Instrument using nitrogen as the adsorbate at 77 K. The specific surface area was calculated by the Brunauer–Emmett–Teller (BET) method in the relative pressure range of 0.05–0.30. Total pore volume was calculated at relative pressure $P/P_o = 0.98$. The pore size distributions were evaluated by using quenched-solid density functional theory, assuming slit-shaped geometry.

2.3 Electrochemical measurements

For electrochemical tests, the electrodes were prepared by mechanically mixing the active material, carbon black (super P), and poly(vinylidenedifluoride) in a 75:15:10 mass ratio to obtain a viscous slurry. The thick semi-solid slurry was screen printed onto the

surface of nickel foam current collector and dried at 100 ˚C overnight. The process utilized was analogous to the conventional planar battery electrode fabrication. The paste was sufficiently viscous as not to coat the Ni foam, rather sinking in only deep enough to promote good mechanical adhesion. After deposition and baking, the active layer very much retained its planar "battery-like" geometry. When the mass loadings employed were 10 mg·cm^{-2}, we found that a second Ni foam layer was necessary to avoid the separation of the active material from the current collector. In that case we mechanically sandwiched the electrode between two foam layers.

A solartron 1470E Multichannel Potentiostat/Cell Test System was used for cyclic voltammetry and galvanostatic charge–discharge measurements. Testing of the individual electrodes was performed in a three-electrode configuration in a 6 mol/L KOH electrolyte. A Pt wire and saturated calomel electrode (SCE) were used as counter and reference electrodes. The cyclic voltammetry (CV) curves were recorded at scan rate from 5 to 200 mV·s^{-1}. The electrochemical tests of asymmetric and symmetric capacitors were performed in a two-electrode cell. The charging/discharging curves were recorded at the current density from 0.5 to 30 A·g^{-1}. The current densities were calculated based on the mass of the positive electrode. The electrochemical impedance spectra were also recorded from 100 kHz to 0.1 Hz at open circuit potential with an ac perturbation of 5 mV.

3. Results and discussion

3.1 Graphene–nickel cobaltite composite electrode

For the synthesis of positive electrode materials, $Ni(NO_3)_2$ and $CoCl_2$ precursors were hydrolyzed in an acid-treated commercial graphene nanoplatelet (TEM images of acid-treated graphene are shown in Fig. S-1 (in the Electronic Supplementary Material (ESM)) suspension in the presence of urea at 100 ˚C. It is important to note that the C/O ratios measured by XPS for graphene before and after HNO_3 treatment were 15.6 and 8.3, respectively (Fig. S-2 (in the ESM)), indicating that the acid treatment process introduces hydrophilic functional groups (–COOH, –C=O, and –OH) at the surface of graphene [45, 46]. During hydrolysis, urea releases hydroxyl ions slowly and uniformly in the suspension, resulting in precipitation of hydroxides. The hydrophilic functional groups on the acid-treated graphene act as anchoring sites for the precipitates. Subsequent calcination in air converts the hydroxides into metal oxides. In the remainder of the manuscript, we term the composites as graphene–nickel cobaltite nanocomposite–*T* (GNCC-*T*), with *T* designating the calcination temperature. The crystal structure of the samples was characterized by using XRD (Fig. 1(a)). In the GNCC-350 all the diffraction peaks can be assigned to spinel $NiCo_2O_4$ except for the peak of graphene at about $2\theta = 26.5°$. For the case of GNCC-250, some NiO is also present, which would necessitate the formation of Co_3O_4. $NiCo_2O_4$ and Co_3O_4 are isostructural, so it is difficult to distinguish between the two phases based on XRD analysis [47]. Therefore, all three phases may coexist in the GNCC-250 specimen.

X-ray photoelectron spectra were recorded to illustrate the near-surface composition and chemical states of the species in the as-synthesized GNCC samples. The Ni 2p and Co 2p spectra of GNCC-250 and GNCC-350 materials are displayed in Fig. 1(b). The Co 2p spectrum consists of two spin-orbit split peaks (i.e., $2p_{3/2}$ at ~780 eV and $2p_{1/2}$ at ~795 eV) and three shake-up satellites (as indicated by arrows in Fig. 1(b)), in accordance with data reported in the Refs. [48–50]. It is difficult to determine the oxidation state merely based on the two main peaks. However, it is generally accepted that the satellite peaks are closely related to the oxidation state of Co cations. The two satellite peaks are located at about 6 eV and 10 eV above the Co $2p_{3/2}$ main peak. The former satellite peak is related to Co^{2+} species while the latter peak is related to Co^{3+} species [48, 49]. We can therefore conclude that both Co^{2+} and Co^{3+} species are present in GNCC samples. The former satellite peak is more obvious in GNCC-250 than in GNCC-350, providing qualitative confirmation of the presence of Co_3O_4. As for the Ni 2p spectrum, there are also two spin-orbit splitting peaks ($2p_{3/2}$ at ~855 eV and $2p_{1/2}$ at ~872 eV) and two satellites peaks, indicating the presence of both Ni^{2+} and Ni^{3+} species [48, 49]. The Ni/Co atomic

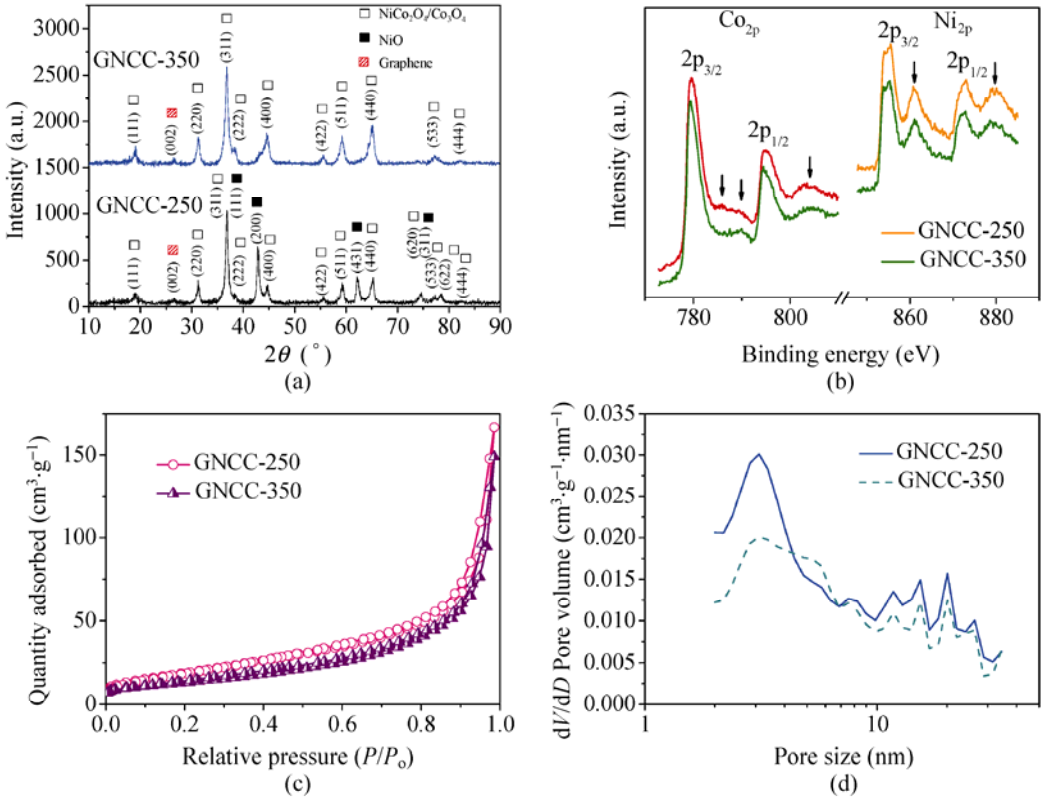

Figure 1 (a) XRD patterns of GNCC samples. (b) Co 2p and Ni 2p XPS spectra of GNCC-250 and GNCC-350, where the arrows denote positions of satellite peaks. (c) Nitrogen adsorption–desorption isotherms and (d) slit-pore pore size distributions of GNCC-250 and GNCC-350 materials

ratio obtained from XPS was 0.84 for GNCC-250, and 0.79 for GNCC-350, highlighting a Ni surface enrichment. As discussed previously, when Ni/Co ≠ 0.5 a charge balance may be achieved either by changing the oxidation states of Ni/Co surface cations, or by substituting surface O^{2-} by hydroxyl groups [48]. XPS analysis highlights the different cation distribution on the surface versus in the bulk. It also provides evidence that there are many cation and oxygen defects in the samples.

The nitrogen adsorption–desorption isotherms and corresponding pore size distributions calculated by using quenched-solid density functional theory for GNCC samples are shown in Fig. 1(c). Type Ⅳ isotherms with hysteresis loops can be seen, and the nitrogen sorption isotherms are similar in appearance to each other. The progressively increasing slope at a relative pressure above roughly 0.6 reflects the capillary condensation of gas in the mesopores. The adsorption of nitrogen increases rapidly at relative pressure close to unity, indicating the presence of large interparticle voids. The BET surface areas of GNCC-250 and GNCC-350 are calculated to be 71 and 55 $m^2 \cdot g^{-1}$, respectively. The total pore volumes of GNCC-250 and GNCC-350 are 0.26 and 0.23 $cm^3 \cdot g^{-1}$. The pore size distribution curves of these two samples are also shown in Fig. 1(d). Both GNCC-250 and GNCC-350 possess small (< 10 nm) and large (> 10 nm) mesopores. However as can be seen from Fig. 1(d), the sample synthesized at 250 ˚C possesses a significantly higher fraction of sub-4 nm mesopores. The porosity is a known consequence of mass loss and volume shrinkage during thermal decomposition. The higher surface area of the GNCC-250 is therefore largely attributable to the finer pore dimensions and a higher total pore volume.

SEM and TEM techniques were employed to investigate the morphology and structure of GNCC samples. Figures 2(a) and 2(b) demonstrate that the electrode morphology consists of needle-like metal oxide nanowires interconnected with a graphene network. The morphology of the nanowires was finer

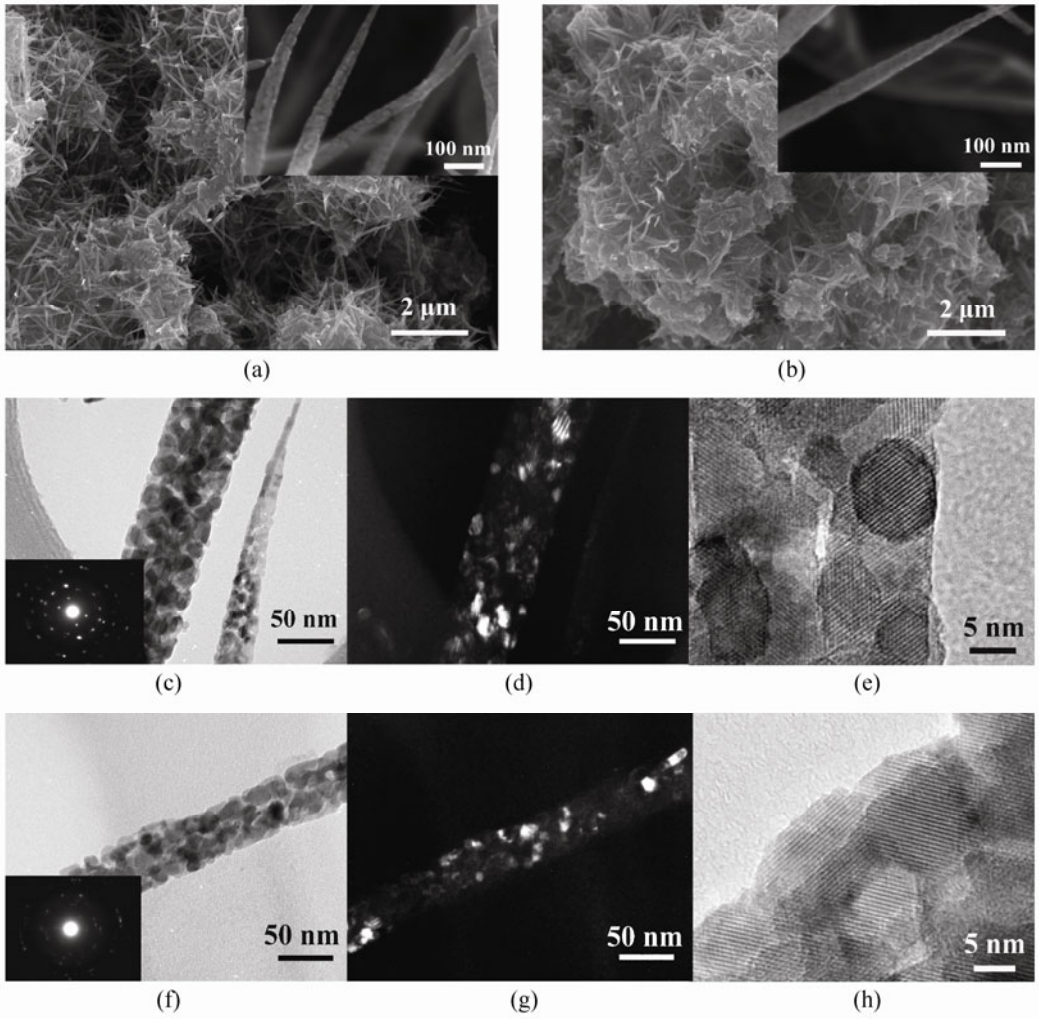

Figure 2 SEM micrographs and high magnification images (inset) of (a) GNCC-250 and (b) GNCC-350 samples. Bright field, dark field and high-resolution TEM images of (c)–(e) GNCC-250 and (f)–(h) GNCC-350 materials

for the specimens synthesized at 250 ˚C. Additional SEM analysis (Fig. S-3 (in the ESM)) further confirms the intimate contact between graphene and the nickel cobaltite nanowires. TEM analysis, shown in Figs. 2(c)–2(h), reveals that the nanowires consist of domains of oxide nanocrystallites. As is known from previous studies on hydrothermal synthesis of cobalt-based oxides, the nanowire precursor is an oriented single crystal [20, 36, 51, 52]. After the thermal decomposition, it can be observed that GNCC-250 exhibits better crystalline continuity from the selected-area electron diffraction pattern, which is a result of the lower calcination temperature. The mean crystallite size was calculated from the experimental XRD patterns using the well-known Scherrer equation. For GNCC-250 and GNCC-350 the average crystallite dimensions were 9.4 and 10.1 nm, respectively. These values agree with the scale of the crystallites imaged in dark field TEM. The higher calcination temperature coarsens the microstructure, resulting in a lower surface area and larger pore diameters.

To evaluate the electrochemical properties of the as-prepared GNCC materials, CV measurements were performed in a 6 mol/L KOH aqueous solution using a three-electrode system. Figure 3(a) shows the CV curves of GNCC-250 and GNCC-350, at a scan rate of 5 $mV \cdot s^{-1}$. Two sets of redox peaks were observed, which reveals that the capacitive characteristic arises mainly from pseudocapacitance. These peaks are responsible for the measured pseudocapacitance. For comparison purposes, graphene–Co_3O_4 composite (labeled as GCC-350) and graphene–NiO composite

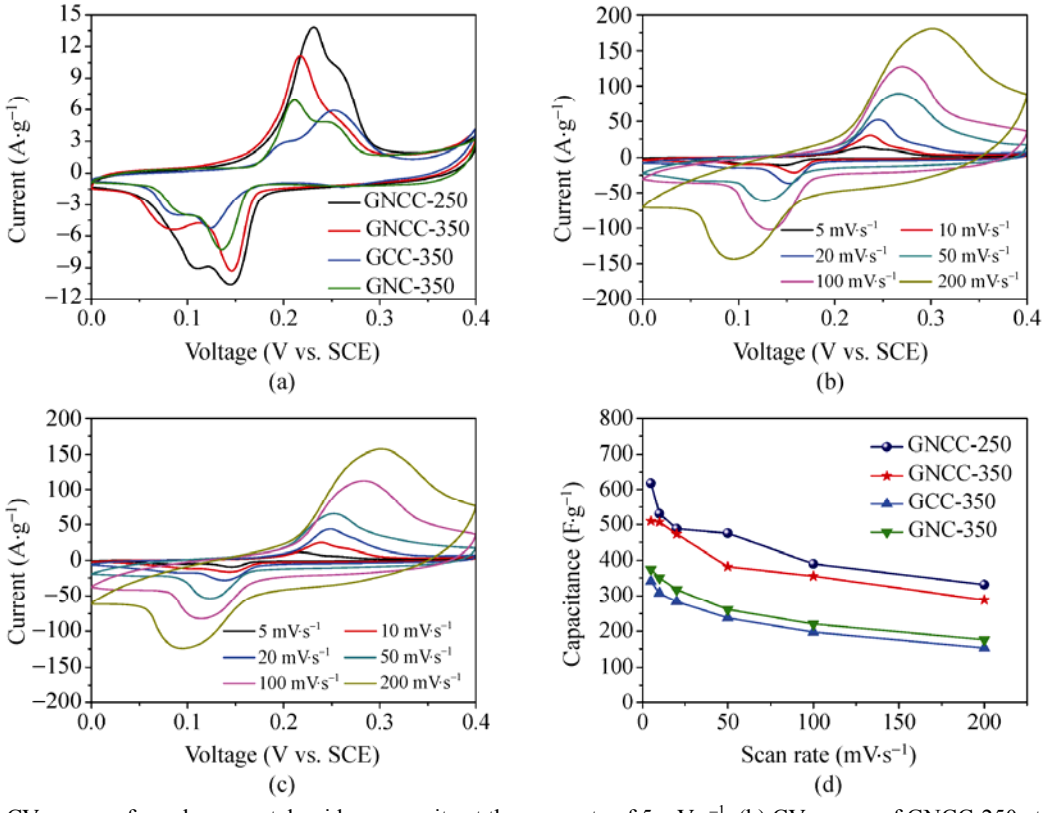

Figure 3 (a) CV curves of graphene–metal oxide composite at the scan rate of 5 mV·s^{-1}. (b) CV curves of GNCC-250 at different scan rates. (c) CV curves of GNCC-350 at different scan rates. (d) Variation of the capacitance of graphene–metal oxide composite with the increase of scan rate

(named as GNC-350) were synthesized via the identical method as for GNCC-350. The CV curves of GCC-350 and GNC-350 are also shown in Fig. 3(a). GCC-350 and GNC-350 also exhibit two pairs of peaks at low scan rate, which can, in part, be due to the presence of oxygen-containing graphene [37]. As compared with those of GNCC-250 and GNCC-350, the CVs of nickel and cobalt oxide display much lower enclosed area corresponding to much lower capacitance. Figures 3(b) and 3(c) display the CV curves of GNCC-250 and GNCC-350 at scan rates from 5 to 200 mV·s^{-1}. At the high scan rates, both electrodes display a single highly broadened oxidation peak. The breadth of the peak is related to the combination of Co^{2+}/Co^{3+} and Ni^{2+}/Ni^{3+} transitions, which do not occur at the same potentials. Increasing scan rate causes a positive shift of the anodic peaks and a negative shift of the cathodic peak. This rate-dependent overpotential is mainly due to the resistance of the electrode. At high scan rates, such as at 200 mV·s^{-1}, the CV curves for the binary oxide are less distorted than those of either oxide [20, 42, 53].

The specific capacitance (C_s) of the electrode was calculated from CV curves according to

$$C_s = \frac{\int I dV}{2\mu m \Delta V}$$

where I is the current (A), V is the potential, ΔV is the potential difference during scan, μ is the scan rate, and m is the mass of the active material. Figure 3(d) displays the specific capacitance of GNCC-250 and GNCC-350 at different scan rates. The average specific capacitance of GNCC-250 was calculated to be 618 F·g^{-1} at a scan rate of 5 mV·s^{-1}, 475 F·g^{-1} at a scan rate of 50 mV·s^{-1}, and 331 F·g^{-1} at a scan rate of 200 mV·s^{-1}. The GNCC-350 electrode demonstrated a specific capacitance of 510 F·g^{-1} at a scan rate of 5 mV·s^{-1}, 382 F·g^{-1} at a scan rate of 50 mV·s^{-1}, and 288 F·g^{-1} at a scan rate of 200 mV·s^{-1}. The percentage of carbon in GNCC-250 and GNCC-350 is about 22–25 wt%, as calculated from the XPS data. Based on the mass of metal oxide, the specific capacitance of GNCC-250

and GNCC-350 can reach to 792 F·g^{-1} and 690 F·g^{-1}. It is critical to point out that while a higher specific capacitance has been previously reported in the Ref. for nickel cobaltite [35], the mass loading utilized there was more than an order of magnitude lower (0.4 mg·cm^{-2}). Given the near commercial-level of electrode mass loading employed in the current study (10 mg·cm^{-2}), these specific capacitance values are very favorable.

3.2 Asymmetric electrochemical capacitor

To further evaluate the graphene–nickel cobaltite composite for real device application, we fabricated asymmetric capacitors using GNCC-250 and a commercially available activated carbon (labeled as activated carbon (AC), Norit™, surface area: 1930 m^2·g^{-1}, pore volume: 1.17 cm^3·g^{-1}) as positive and negative electrodes with a high mass loading of 10 mg·cm^{-2}. The SEM image, nitrogen sorption isotherm, and CV curves of activated carbon at the scan rate from 5 to 200 mV·s^{-1} are displayed in Figs. S-4–S-6 (in the ESM). The specific capacitance of activated carbon is 171 F·g^{-1} at a scan rate of 5 mV·s^{-1}, with a capacity retention ratio of 64% at 200 mV·s^{-1}, showing the fast ion-transport characteristic of electric double-layer storage. Based on the electrochemical analysis of GNCC-250 and AC electrodes, it is expected that the operating cell voltage of an asymmetric capacitor could be extended to 1.4 V, if the cell voltage can be expressed as the sum of the potential range for GNCC-250 and AC materials. We used different mass ratios of positive and negative electrodes ($M_{GNCC\text{-}250}$:M_{AC} = 1:1, 1:2, 1:3, and 1:4) to evaluate the electrochemical performance of these asymmetric capacitors.

Figure 4(a) shows the CV data for the asymmetric electrochemical capacitor with different mass ratios, at a scan rate of 5 mV·s^{-1}. With a mass ratio of 1:1, the fabricated asymmetric capacitor exhibits reasonable capacitive behavior with a quasi-rectangular CV curve. However with increasing mass ratios the device capacitance is greatly enhanced. At the high scan rate of 100 mV·s^{-1}, the CV curve is only slightly distorted (Fig. 4(b)), which demonstrates the desirable fast charging/discharging characteristic of the devices. To further evaluate the performance of the cell, galvanostatic charge–discharge testing was measured at various current densities. Figure 4(c) shows the charge–discharge curves of the asymmetric capacitor with different mass ratios, at a current density of 1 A·g^{-1}. It can be seen that the discharge curve is symmetric with its corresponding charge counterpart, demonstrating excellent electrochemical reversibility and good coulombic efficiency. The specific capacitance (C_c) was evaluated from charging/discharging curves according to [8]

$$C_c = \frac{I\Delta t}{\Delta V}\left(\frac{1}{m_+}+\frac{1}{m_-}\right)$$

where I is the current (A), Δt is the discharging time, ΔV is the voltage after IR drop, and m_+ and m_- is the mass of positive electrode and negative electrode. The specific capacitance of the asymmetric capacitor operated with different mass ratios is plotted in Fig. 4(d). The specific capacitance of the asymmetric capacitor increased with increasing mass ratio, up to a ratio of 1:3, remaining stable after that. This indicates that further increasing the mass of the activated carbon is not helpful, since the positive electrode now becomes the limitation. Overall the best combination of capacitance and rate capability is found with a mass ratio of 1:3. The calculated specific capacitance of the asymmetric capacitor with mass ratio of 1:3 is 288 F·g^{-1} at 0.5 A·g^{-1}, and 173 F·g^{-1} at 30 A·g^{-1}, demonstrating an excellent capacity retention ratio of 60%.

Ragone plots relating the energy density to the power density are an efficient way to evaluate the performance of electrochemical capacitors. To demonstrate the operational characteristics, the energy density (E) and power density (P) were calculated from the galvanostatic charge–discharge curves (Fig. 4(e)) according to the following equations [8, 9]

$$E = \frac{1}{2}CV^2 = \frac{1}{8}MC_cV^2$$

$$P = \frac{E}{t}$$

where V is the voltage of the capacitor after IR drop, t is the discharge time, M is the total mass of positive and negative electrode, and C is the total capacitance of the asymmetric capacitor ($C_c = 4C/M$). For comparison, we also fabricated two-electrode GNCC//GNCC and AC//AC symmetric capacitors with mass ratio of 1:1.

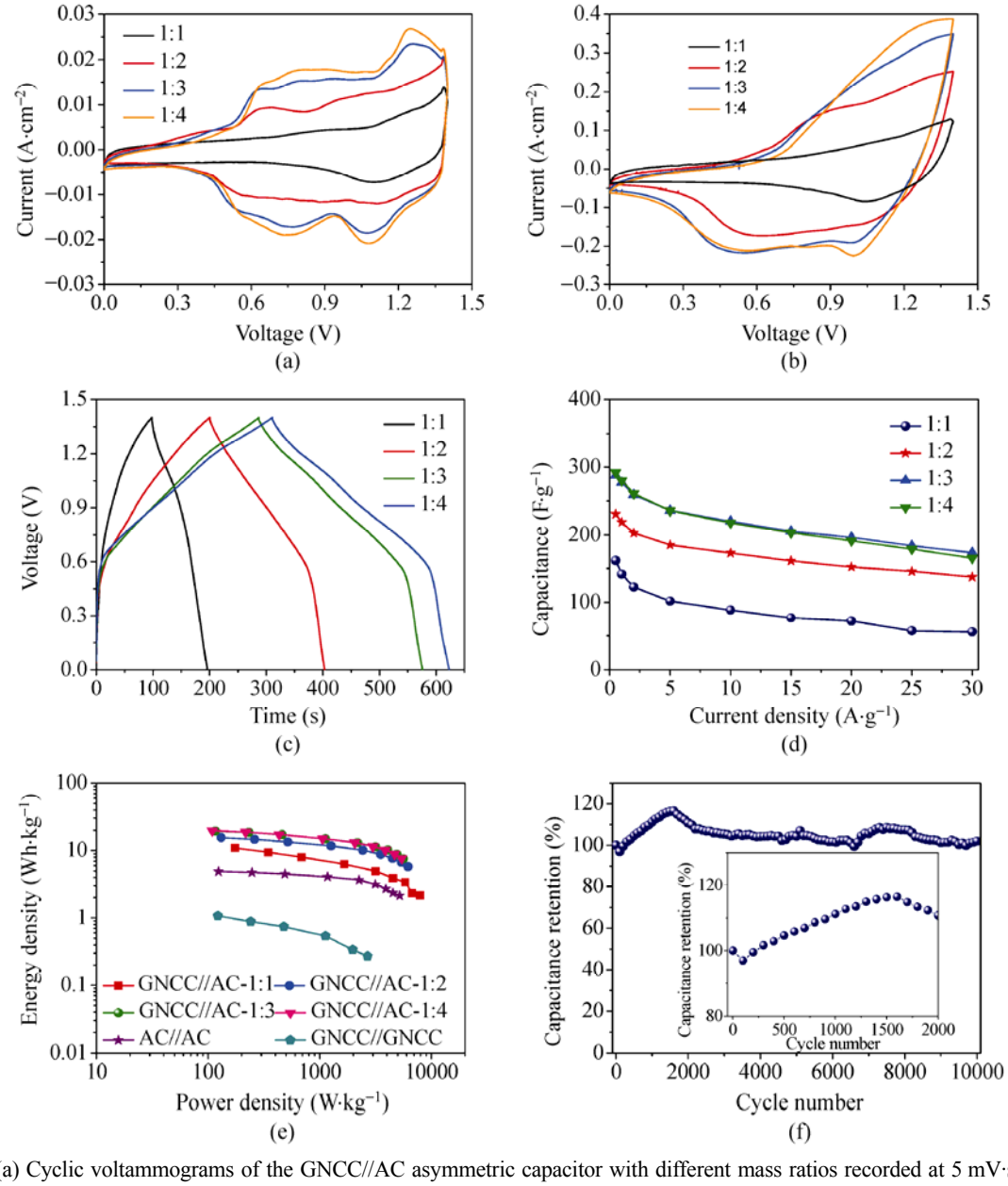

Figure 4 (a) Cyclic voltammograms of the GNCC//AC asymmetric capacitor with different mass ratios recorded at 5 $mV \cdot s^{-1}$. (b) Cyclic voltammograms of the GNCC//AC asymmetric capacitor with different mass ratios recorded at 100 $mV \cdot s^{-1}$. (c) Galvanostatic charging–discharging profiles of the asymmetric capacitor with different mass ratios at 1 $A \cdot g^{-1}$. (d) Variation of the capacitance of the asymmetric capacitor operated at different mass ratios with the increase of current density. (e) Ragone plots related to energy density and power density of GNCC//AC asymmetric capacitor with various mass ratios, GNCC//GNCC and AC//AC symmetric capacitors. (f) Capacitance retention versus cycle number at 10 $A \cdot g^{-1}$

These capacitors were tested in the voltage range between 0 and 1.0 V. The GNCC//GNCC symmetric capacitor only exhibited a very low energy density of 1.07 $Wh \cdot kg^{-1}$. Although GNCC showed excellent electrochemical performance in a three-electrode system, its performance in the two-electrode configuration was inferior. This is likely due to the matching problem caused by employing the same metal oxide electrode with a narrow electrochemical window. It is clear to see that the energy–power density curve of asymmetric capacitor with mass ratio of 1:2, 1:3, and 1:4 is as flat as AC//AC symmetric capacitor, indicating that the asymmetric capacitor can deliver high power comparable to porous carbon

materials. This opens the way for high-rate performance supercapacitors by using metal oxides as electrodes. Take the asymmetric capacitor with mass ratio of 1:3 as an example; our asymmetric capacitor can reach an energy density of about 19.5 $Wh \cdot kg^{-1}$, and is capable of delivering a reasonable energy density of 7.57 $Wh \cdot kg^{-1}$ and a high power density of about 5600 $W \cdot kg^{-1}$ at the current density of 30 $A \cdot g^{-1}$.

Extended electrochemical cycling life is a critical requirement for supercapacitor devices. Cycling performance of the GNCC//AC asymmetric capacitor with high mass loading operated at 1.4 V was evaluated using galvanostatic charge/discharge cycling at 10 $A \cdot g^{-1}$ over 10000 cycles. The cycling stability is presented in Fig. 4(f). The specific capacitance showed a decrease after the initial 100 cycles (retaining 97% of its initial capacitance), which can be attributed to pulverization and wettability issues [54]. Subsequent cycling actually caused an increase in the capacitance up to 1600 cycles. This is likely related to a cycling-induced improvement in the surface wetting of the electrode, leading to more electroactive surface area. After 10000 cycles the asymmetric capacitor demonstrates outstanding cycling stability, showing no capacitance fade from its initial value (the capacitance actually improved to 102% of its initial value). This would be a positive result for a faradaic-based system at any mass loading, but is especially promising for the electrode configuration explored here.

Electrochemical impedance spectroscopy analysis was performed on the asymmetric capacitor after the 1st, 2000th, and 10000th cycle, in the frequency range of 100 kHz–0.1 Hz. The Nyquist plots are presented in Fig. S-7 (in the ESM). At very high frequencies, the real axis intercept represents the sum of the ionic resistance of electrolyte, the active material resistance, and the contact resistance of the interface between active material and current collector [9]. This equivalent series resistance (ESR) of the electrodes stays remarkably low throughout voltage cycling. The ESR values were 0.63, 0.34, and 0.30 Ω after the 1st, 2000th, and 10000th cycle. As will be discussed shortly, we attribute such low ESR values to the presence of the highly electrically conductive graphene "skeleton". The semicircle in the high-frequency range is due to the charge-transfer resistance. The charge transfer resistances were increased, being 0.40, 0.52, and 2.52 Ω after the 1st, 2000th, and 10000th cycle, which is probably due to the corrosion of the current collector caused by the dissolved oxygen in electrolyte and the enhanced pseudocapacitance [9]. The most significant difference could be found in the low-frequency range, with the length of the 45° Warburg segment increasing with cycling. This is generally attributed to a progressive increase in the diffusional resistance faced by the electrolyte ions. This in turn may be related to cycling-induced changes in the pore structure of either electrode, with the interconnected porosity becoming more tortuous.

The superior cycling stability and high energy–power densities of the 10 $mg \cdot cm^{-2}$ loaded GNCC//AC asymmetric capacitor may be ascribed to several electrode design and microstructural factors. During charging/discharging cycling, faradaic electrodes tend to degrade by microstructural agglomeration. This leads to progressively lower electroactive surface areas and higher equivalent series resistances. Our hypothesis is that the remarkable cycling stability of the GNCC electrode is due to its nanoscale graphene "skeleton" that continues to provide a high-conductivity electrical path while anchoring the microstructure and reducing the rate of coarsening. The densely dispersed graphene sheets in the nanocomposite serve as highly electrically conductive paths within the microstructure, reducing the overall internal resistance of the thick electrodes. This not only promotes enhanced cycling stability, but also the favorable rate capability and the high power density. Since the graphene "skeleton" is essentially the same in GNCC, GCC, and GNC specimens, they all possess similarly excellent scan-rate dependent capacity retention.

The energy density of electrochemical capacitors is proportional to the square of the cell voltage. Therefore the enhancement in the energy density of an asymmetric device is first of all due to the enlarged operation voltage window as compared to the symmetric GNCC//GNCC and AC//AC capacitors. By employing a mixed oxide, with multiple oxidation states, the GNCC electrode pseudocapacitance is maximized. A key attribute leading to the high specific capacitance of GNCC electrodes are multiple redox reactions in $NiCo_2O_4$ [35], as opposed to a single

redox reaction expected for Co_3O_4 or NiO within the voltage range of testing. Mixed oxides are also known to possess improved electrical conductivity relative to their binary counterparts [35]. Another key feature is the nanoscale crystallite size combined with the high levels of mesoporosity, especially in the GNCC-250 electrode. The large volume of mesopores will provide ample surface area for the redox reactions, while allowing facile electrolyte access. Moreover, the nanoscale crystallite and aggregate dimensions of the nickel cobaltite will provide an abundance of faradic reaction sites for the adsorbed ions. In the AC electrode, electric double-layer is the main energy storage mechanism, which is favorable for high power and long cycle life. For asymmetric capacitors, it is important not to change a good supercapacitor into a mediocre battery due to the existence of a pseudocapacitive electrode [2]. The high rate capability of both positive and negative electrodes ensures that our asymmetric capacitor can achieve both high energy density and power density. A combination of these favorable characteristics allowed us to fabricate high performance electrodes with a higher mass loading than what is normally utilized in academic studies, paving the way for the application of such advanced materials in commercial devices.

4. Conclusions

We have created a high performance asymmetric electrochemical supercapacitor with each planar electrode being based on a mass loading of 10 $mg \cdot cm^{-2}$ per real surface area. A graphene–nickel cobaltite nanocomposite is utilized as a positive electrode, and an activated carbon is employed as a negative electrode. Even with such a high mass loading the ultracapacitor exhibits favorable energy and power densities, and 102% capacitance retention at over 10000 cycles. The capacitance of the positive electrode was 618 $F \cdot g^{-1}$ at 5 $mV \cdot s^{-1}$ and 331 $F \cdot g^{-1}$ at 200 $mV \cdot s^{-1}$. Electrodes consisting of graphene–Co_3O_4 or graphene–NiO nanocomposites synthesized via identical methods, yielded much inferior values of 340 and 375 $F \cdot g^{-1}$, respectively. A two electrode asymmetric capacitor based on GNCC and AC displayed an energy density in the range of 19.5 $Wh \cdot kg^{-1}$ when operated at 1.4 V. When operated with a positive to negative electrode mass ratio of 1:3, the system is capable of delivering a power density of about 5600 $W \cdot kg^{-1}$ at an energy density of 7.6 $Wh \cdot kg^{-1}$. This superior electrochemical performance of GNCC is ascribed to several microstructural features including the presence of a nanoscale graphene network "skeleton" that maintains excellent electrical conductivity of the electrode throughout cycling; a rich number of faradaic reactions on the nickel cobaltite; and a highly porous structure that improves ion transport and maximizes the amount of electrolyte-exposed surface.

Acknowledgements

This work was funded by Natural Sciences and Engineering Research Council of Canada (NSERC) Discovery and National Institute for Nanotechnology (NINT) National Research Council (NRC).

Electronic Supplementary Material: Supplementary material (TEM images of acid-treated commercial graphene, XPS data of commercial graphene before and after acid treatment, SEM images of graphene–nickel cobaltite, SEM image, nitrogen sorption isotherm, and CV curves of activated carbon, and Nyquist plot of asymmetric capacitor) is available in the online version of this article at http://dx.doi.org/10.1007/s12274-012-0246-X.

References

[1] Conway, B. E. *Electrochemical Supercapacitors, Scientific Fundamentals and Technological Applications*; Kluwer Academic/Plenum: New York, 1999.

[2] Simon, P.; Gogotsi, Y. Materials for electrochemical capacitors. *Nat. Mater*. **2008**, *7*, 845–854.

[3] Zhu, Y.; Murali, S.; Stoller, M. D.; Ganesh, K. J.; Cai, W.; Ferreira, P. J.; Pirkle, A.; Wallace, R. M.; Cychose, K. A.; Thommes, M. et al. Carbon-based supercapacitors produced by activation of graphene. *Science* **2011**, *332*, 1537–1541.

[4] Hall, P. J.; Mirzaeian, M.; Isobel Fletcher, S.; Sillars, F. B.; Rennie, A. J. R.; Shitta-Bey, G. O.; Wilson, G.; Cruden, A.; Carter, R. Energy storage in electrochemical capacitors: Designing functional materials to improve performance. *Energy Environ. Sci.* **2010**, *3*, 1238–1251.

[5] Long, J. W.; Bélanger, D.; Brousse, T.; Sugimoto, W.; Sassin, M. B.; Crosnier, O. Asymmetric electrochemical capacitors-stretching the limits of aqueous electrolytes. *MRS Bull.* **2011**, *36*, 513–522.

[6] Demarconnay, L.; Raymundo-Piñero, E.; Béguin, F. Adjustment of electrodes potential window in an asymmetric carbon/MnO_2 supercapacitor. *J. Power Sources* **2011**, *196*, 580–586.

[7] Qu, Q.; Zhang, P.; Wang, B.; Chen, Y.; Tian, S.; Wu, Y.; Holze, R. Electrochemical performance of MnO_2 nanorods in neutral aqueous electrolytes as a cathode for asymmetric supercapacitors. *J. Phys. Chem. C* **2009**, *113*, 14020–14027.

[8] Chen, P. C.; Shen, G.; Shi, Y.; Chen, H.; Zhou, C. Preparation and characterization of flexible asymmetric supercapacitors based on transition-metal-oxide nanowire/single-walled carbon nanotube hybrid thin-film electrodes. *ACS Nano* **2010**, *4*, 4403–4411.

[9] Fan, Z.; Yan, J.; Wei, T.; Zhi, L.; Ning, G.; Li, T.; Wei, F. Asymmetric supercapacitors based on graphene/MnO_2 and activated carbon nanofiber electrodes with high power and energy density. *Adv. Funct. Mater.* **2011**, *21*, 2366–2375.

[10] Brousse, T.; Taberna, P. L.; Crosnier, O.; Dugas, R.; Guillemet, P.; Scudeller, Y.; Zhou, Y.; Favier, F.; Bélanger, D.; Simon, P. Long-term cycling behavior of asymmetric activated carbon/MnO_2 aqueous electrochemcial supercapacitor. *J. Power Sources* **2007**, *173*, 633–641.

[11] Wang, H.; Gao, Q.; Hu, J. Asymmetric capacitor based on superior porous Ni–Zn–Co oxide/hydroxide and carbon electrode. *J. Power Sources* **2010**, *195*, 3017–3024.

[12] Du, X.; Wang, C.; Chen, M.; Jiao, Y.; Wang, J. Electrochemical performances of nanoparticle Fe_3O_4/activated carbon supercapacitor using KOH electrolyte solution. *J. Phys. Chem. C* **2009**, *113*, 2643–2646.

[13] Wang, D. W.; Li, F.; Liu, M.; Lu, G. Q.; Cheng, H. M. 3D aperiodic hierarchical porous graphitic carbon material for high-rate electrochemical capacitive energy storage. *Angew. Chem. Int. Ed.* **2007**, *47*, 373–376.

[14] Chmiola, J.; Yushin, G.; Gogotsi, Y.; Portet, C.; Simon, P.; Taberna, P. L. Anomalous increase in carbon capacitance at pore sizes less than 1 nanometer. *Science* **2006**, *313*, 1760–1763.

[15] Rose, M.; Korenblit, Y.; Kockrick, E.; Borchardt, L.; Oschatz, M.; Kaskel, S.; Yushin, G. Hierarchical micro- and mesoporous carbide-derived carbon as a high-performance electrode material in supercapacitors. *Small* **2011**, *7*, 1108–1117.

[16] Hulicova-Jurcakova, D.; Puziy, A. M.; Poddubnaya, O. I.; Suárez-García, F.; Tascón, J. M. D.; Lu, G. Q. Highly stable performance of supercapacitors from phosphous-enriched carbons. *J. Am. Chem. Soc.* **2009**, *131*, 5026–5027.

[17] Hu, C. C.; Chen, W. C.; Chang, K. H. How to achieve maximum utilization of hydrous ruthenium oxide for supercapacitors. *J. Electrochem. Soc.* **2004**, *151*, A281–A290.

[18] Cheng, H.; Lu, Z. G.; Deng, J. Q.; Chung, C. Y.; Zhang, K.; Li, Y. Y. A facile method to improve the high rate capability of Co_3O_4 nanowire array electrodes. *Nano Res.* **2010**, *3*, 895–901.

[19] Zhang, L.; Holt, C. M. B.; Luber, E. J.; Olsen, B. C.; Wang, H.; Danaie, M.; Cui, X.; Tan, X.; Liu, V. W.; Kalisvaart, W. P.; Mitlin, D. High rate electrochemical capacitors from three-dimensional arrays of vanadium nitride functionalized carbon nanotubes. *J. Phys. Chem. C* **2011**, *115*, 23381–24393.

[20] Wang, H.; Zhang, L.; Tan, X.; Holt, C. M. B.; Zahiri, B.; Olsen, B. C.; Mitlin, D. Supercapacitive properties of hydrothermally synthesized Co_3O_4 nanostructures. *J. Phys. Chem. C* **2011**, *115*, 17599–17605.

[21] Wei, T. Y.; Chen, C. H.; Chang, K. H.; Lu, S. Y.; Hu, C. C. Cobalt oxide aerogels of ideal supercapacitive properties prepared with an epoxide synthetic route. *Chem. Mater.* **2009**, *21*, 3228–3233.

[22] Lei, Y.; Daffos, B.; Taberna, P. L.; Simon, P.; Favier, F. MnO_2-coated Ni nanorods: Enhanced high rate behavior in pseudo-capacitive supercapacitor. *Electrochim. Acta* **2010**, *55*, 7454–7459.

[23] Zhu, J. W.; Chen, S.; Zhou, H.; Wang, X. Fabrication of a low defect density graphene–nickel hydroxide nanosheet hybrid with enhanced electrochemical performance. *Nano Res.* **2012**, *5*, 11–19.

[24] Wang, H.; Casalongue, H. S.; Liang, Y.; Dai, H. $Ni(OH)_2$ nanoplates grown on graphene as advanced electrochemical pseudocapacitor materials. *J. Am. Chem. Soc.* **2010**, *132*, 7472–7477.

[25] Liu, X.; Pickup, P. G. Carbon fabric supported manganese and ruthenium oxide thin films for supercapacitors. *J. Electrochem. Soc.* **2011**, *158*, A241–A249.

[26] Zhu, Y.; Murali, S.; Cai, W.; Li, X.; Suk, J. W.; Potts, J. R.; Ruoff, R. S. Graphene and graphene oxide: Synthesis, properties, and applications. *Adv. Mater.* **2010**, *22*, 3906–3924.

[27] Stoller, M. D.; Park, S.; Zhu, Y.; An, J.; Ruoff, R. S. Graphene-based ultracapacitors. *Nano Lett.* **2008**, *8*, 3498–3502.

[28] Lei, Z.; Lu, L.; Zhao, X. S. The electrocapacitive properties of graphene oxide reduced by urea. *Energy Environ. Sci.* **2012**, *5*, 6391–6399.

[29] Chen, S.; Zhu, J.; Wang, X. One–step synthesis of graphene–cobalt hydroxide nanocomposites and their electrochemical properties. *J. Phys. Chem. C* **2010**, *114*, 11829–11834.

[30] Wang, H.; Liang, Y.; Mirfakhrai, T.; Chen, Z.; Casalongue, H. S.; Dai, H. Advanced asymmetrical supercapacitors based on graphene hybrid materials. *Nano Res.* **2011**, *4*, 729–736.

[31] Yan, J.; Wei, T.; Shao, B.; Fan, Z.; Qian, W.; Zhang, M.; Wei, F. Preparation of a graphene nanosheet/polyaniline composite with high specific capacitance. *Carbon* **2010**, *48*, 487–493.

[32] Lv, W.; Sun, F.; Tang, D. M.; Fang, H. T.; Liu, C.; Yang, Q. H.; Cheng, H. M. A sandwich structure of graphene and nickel oxide with excellent supercapacitive performance. *J. Mater. Chem.* **2011**, *21*, 9014–9019.

[33] Zhou, W.; Liu, J.; Chen, T.; Tan, K. S.; Jia, X.; Luo, Z.; Cong, C.; Yang, H.; Li, C. M.; Yu, T. Fabrication of Co_3O_4–reduced graphene oxide scrolls for high–perfromance supercapacitor electrodes. *Phys. Chem. Chem. Phys.* **2011**, *13*, 14462–14465.

[34] Yan, J.; Wei, T.; Qiao, W.; Shao, B.; Zhao, Q.; Zhang, L.; Fan, Z. Rapid microwave–assisted synthesis of graphene nanosheet/Co_3O_4 composite for supercapacitors. *Electrochim. Acta* **2010**, *55*, 6973–6978.

[35] Wei, T. Y.; Chen, C. H.; Chien, H. C.; Lu, S. Y.; Hu, C. C. A cost–effective supercapacitor material of ultrahigh specific capacitances: Spinel nickel cobaltite aerogels from an epoxide–driven sol–gel process. *Adv. Mater.* **2010**, *22*, 347–351.

[36] Wang, H.; Gao, Q.; Jiang, L. Facile approach to prepare nickel cobaltite nanowire materials for supercapacitors. *Small* **2011**, *7*, 2454–2459.

[37] Wang, H. W.; Hu, Z. A.; Chang, Y. Q.; Chen, Y. L.; Wu, H. Y.; Zhang, Z. Y.; Yang, Y. Y. Design and synthesis of $NiCo_2O_4$–reduced graphene oxide composites for high performance supercapacitors. *J. Mater. Chem.* **2011**, *21*, 10504–10511.

[38] Wu, Z. S.; Ren, W.; Wang, D. W.; Li, F.; Liu, B.; Cheng, H. M. High-energy MnO_2 nanowire/graphene and graphene asymmetric electrochemical capacitors. *ACS Nano* **2010**, *4*, 5835–5842.

[39] Zhang, J.; Jiang, J.; Li, H.; Zhao, X. S. A high–performance asymmetric supercapacitor fabricated with graphene–based electrodes. *Energy Environ. Sci.* **2011**, *4*, 4009–4015.

[40] Hu, L.; Choi, J. W.; Yang, Y.; Jeong, S.; La Mantia, F.; Cui, L. F.; Cui. Y. Highly conductive paper for energy–storage devices. *Proc. Natl. Acad. Sci. USA.* **2009**, *106*, 21490–21494.

[41] Yang, L.; Cheng, S.; Ding, Y.; Zhu, X.; Wang, Z. L.; Liu, M. Hierarchical network architectures of carbon fiber paper supported cobalt oxide nanonet for high–capacity pseudocapacitors. *Nano Lett.* **2012**, *12*, 321–325.

[42] Lu, Z.; Yang, Q.; Zhu, W.; Chang, Z.; Liu, J.; Sun, X.; Evans, D. G.; Duan, X. Hierarchical Co_3O_4@Ni–Co–O supercapacitor electrodes with ultrahigh specific capacitance per area. *Nano Res.* **2012**, *5*, 369–378.

[43] Stoller, M. D.; Ruoff, R. S. Best practice methods for determining an electrode material's performance for ultracapacitors. *Energy Environ. Sci.* **2010**, *3*, 1294–1301.

[44] Gogotsi, Y.; Simon, P. True performance metrics in electrochemical energy storage. *Science* **2011**, *334*, 917–918.

[45] Kim, U. J.; Furtado, C. A.; Liu, X.; Chen, G.; Eklund, P. C. Raman and IR spectroscopy of chemically processed single–walled carbon nanotubes. *J. Am. Chem. Soc.* **2005**, *127*, 15437–15445.

[46] Mishra, A. K.; Ramaprabhu, S. Functionalized graphene–based nanocomposites for supercapacitor application. *J. Phys. Chem. C* **2011**, *115*, 14006–14013.

[47] Cabo, M.; Pellicer, E.; Rossinyol, E.; Estrader, M.; López-Ortega, A.; Nogués, J.; Castell, O.; Suriñach, S.; Baró, M. D. Synthesis of compositionally graded nanocast NiO/$NiCo_2O_4$/Co_3O_4 mesoporous composites with tunable magnetic properties. *J. Mater. Chem.* **2010**, *20*, 7021–7028.

[48] Marco, J. F.; Gancedo, J. R.; Gracia, M.; Gautier, J. L.; Ríos, E.; Berry, F. J. Characterization of the nickel cobaltite, $NiCo_2O_4$, prepared by several methods: An XRD, XANES, EXAFS, and XPS study. *J. Solid State Chem.* **2000**, *153*, 74–81.

[49] Marco, J. F.; Gancedo, J. R.; Gracia, M.; Gautier, J. L.; Ríos, E. I.; Palmer, H. M.; Greaves, C.; Berry, F. J. Cation distribution and magnetic structure of the ferrimagnetic spinel $NiCo_2O_4$. *J. Mater. Chem.* **2001**, *11*, 3087–3093.

[50] Zhu, J.; Gao, Q. Mesoporous MCo_2O_4 (M = Cu, Mn, and Ni) spinels: Structural replication, characterization and catalytic application in CO oxidation. *Microporous. Mesoporous. Mat.* **2009**, *124*, 144–152.

[51] Tian, L.; Zou, H.; Fu, J.; Yang, X.; Wang, Y.; Guo, H.; Fu, X.; Liang, C.; Wu, M.; Shen, P. K.; Gao, Q. Topotactic conversion route to mesoporous quasi–single–crystalline Co_3O_4 nanobelts with optimizable electrochemcial performance. *Adv. Funct. Mater.* **2010**, *20*, 617–623.

[52] Wang, Y.; Xia, H.; Lu, L.; Lin, J. Excellent performance in lithium–ion battery anodes: Rational synthesis of $Co(CO_3)_{0.5}(OH)0.11H_2O$ nanobelt array and its conversion into mesoporous and single–crystal Co_3O_4. *ACS Nano* **2010**, *4*, 1425–1432.

[53] Lang, J. W.; Kong, L. B.; Wu, W. J.; Luo, Y. C.; Kang, L. Facile approach to prepare loose–packed NiO nano–flakes materials for supercapacitors. *Chem. Commun.* **2008**, 4213–4215.

[54] Hu, G.; Li, C.; Gong, H. Capacitance decay of nano porous nickel hydroxide. *J. Power Sources* **2010**, *195*, 6977–6981.